Turkish Journal of Electrical Engineering & Computer Sciences

http://journals.tubitak.gov.tr/elektrik/

Research Article

Turk J Elec Eng & Comp Sci
(2016) 24: 2220 – 2238

doi:10.3906/elk-1310-102

Optimal digital control of a three-phase four-leg voltage source inverter

Ayhan ÖZDEMİR, Zekiye ERDEM*
Department of Electrical and Electronics Engineering, Sakarya University, Sakarya, Turkey

Received: 14.10.2013 • **Accepted/Published Online:** 06.07.2014 • **Final Version:** 15.04.2016

Abstract: This paper presents a three-dimensional (3-D) space vector pulse width modulation (SVPWM) technique via a 4 × 4 orthonormal transformation matrix that has been used as a new approach in controlling a three-phase four-leg voltage source inverter (VSI). A fully optimal digital control scheme for the closed-loop regulation of the three-phase four-leg VSI has been used to synthesize a sinusoidal waveform with the help of the proposed method. Discrete-time modelling of each phase has been obtained independently in *abc* reference frame, and its optimal controller has been designed using a predefined performance index. A DSP-based controlled three-phase four-leg prototype VSI has been designed to verify the proposed discrete time modelling and the control scheme. The simulations and the real-time experiments show that satisfactory results have been obtained for the modelling of the three-phase four-leg VSI in *abc* reference frame and the 3-D SVPWM technique via 4 × 4 orthonormal transformation matrix at 20 kHz switching frequency.

Key words: Three-phase four-leg, optimal control, voltage source converter, 3-D SVPWM, four-leg voltage source converter, transformation matrix

1. Introduction

Voltage source inverters (VSIs) are commonly used in industrial applications such as active power filters, uninterruptible power supply (UPS), pulse width modulation (PWM) rectifiers, and AC motor drives. Thyristors and topologies with transformers are used in the old technology for UPS applications, while IGBTs and topologies without transformers are used in the new technology [1]. Several studies exist for modelling and control of three-phase four-leg VSIs in the literature. A control strategy based on the symmetrical components has been discussed in [2]. The control vector calculated by the digital controller inside the dodecahedron defined by the boundaries of the inverter linear operating range in *abc* coordinates has been presented in [3]. A different approach for the three-phase four-leg VSI based on the separation of the control of the fourth leg from that of the other phases has been offered in [4]. A digital control strategy to control the whole system with a microcontroller based on a load current observer has been introduced in [5]. A study of synchronous rotating control strategy based on the decomposition sequence has been given [6]. A dynamic reference voltage hysteresis control scheme has been introduced in [7]. A control strategy based on disturbance observer reduced order and disturbance feed forward in the state space has been offered in [8]. The state-feedback-with-integral and repetitive control for a single-phase half-bridge UPS inverter [9], a model reference controller with a repetitive control action for a single-phase full-bridge UPS inverter [10], and the algorithm of digital multiple feedback control [11,12] are the

*Correspondence: zekiye@sakarya.edu.tr

methods existing in the literature for one phase VSIs. The optimal linear quadratic regulator (LQR) is used for controlling an interleaved boost converter [13]. Five different schemes for digital feedback control of the PWM inverter are proposed and compared through simulations and experiments in [14]. A three-phase VSI has been implemented topologically by using either a three-phase three-leg inverter with split DC link capacitors or a three-phase four-leg inverter. In this study, the topology corresponding to the power circuit used in the simulations and real-time applications of the three-phase four-leg VSI is the same as the one given in [15–18]. Space vector pulse width modulation (SVPWM) is carried out by using either 2-D SVPWM or 3-D SVPWM methods according to the topology [15,16,18–21]. Pulse width modulation algorithms can be used by making $abc \rightarrow \alpha\beta$ coordinate transformation [16,18–20] or directly in abc coordinates [22,23]. All 3-D SVPWM available strategies using $abc \rightarrow \alpha\beta 0$ transformation use a 3×3 $T_{\alpha\beta 0}$ transformation matrix. However, phase-neutral voltages for three phases cannot be expressed independent of each other in terms of modulation indices since there are four modulation indices in a 4-leg inverter. Consequently, inverter output phase-neutral voltages are calculated by subtracting the neutral leg modulation index from the modulation index of each phase.

In this study, $abcn \rightarrow \alpha\beta z$ transformation and 4×4 $T_{\alpha\beta 0z}$ orthonormal transformation matrices are used as a new approach. Therefore, three-phase four-leg inverter output phase-neutral voltages can be defined independent of each other by using four modulation indices. Furthermore, switch states vector expressions $\vec{V}_n$ for all 3×3 $T_{\alpha\beta 0}$ transformation matrices used in the literature and the proposed 4×4 $T_{\alpha\beta 0z}$ orthonormal transformation matrix have been provided in a table for 3-D SVPWM strategies.

2. Modelling of VSI in *abc* coordinates system

In this section, a continuous-time state space model of a three-phase four-leg VSI will be obtained first. Next, the full state feedback and feed forward integral controlled augmented discrete-time state space model will be given.

2.1. Modelling of VSI

Three-phase four-leg voltage source inverter topology with LC filter output is given in Figure 1.

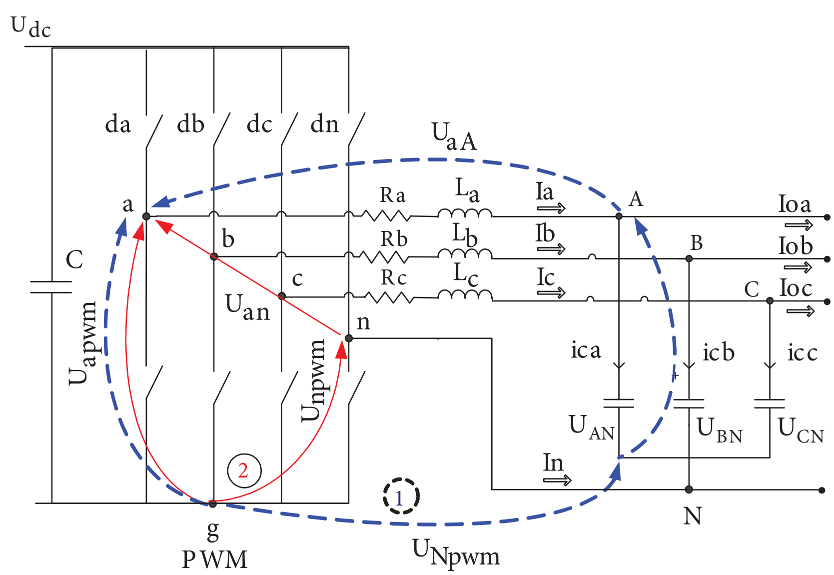

Figure 1. Three-phase four-leg VSI topology.

In Figure 1, the loop and its variables corresponding only to *phase-a* are indicated in order to avoid confusion. If the KVL is applied to the loops 1 and 2, dynamic equations of the three-phase four-leg VSI are obtained as

$$\begin{aligned} U_{apwm}(t) &= L_a \tfrac{di_a(t)}{dt} + R_a i_a(t) + U_{AN}(t) + U_{Npwm}(t) \\ U_{bpwm}(t) &= L_b \tfrac{di_b(t)}{dt} + R_b i_b(t) + U_{BN}(t) + U_{Npwm}(t) \\ U_{cpwm}(t) &= L_c \tfrac{di_c(t)}{dt} + R_c i_c(t) + U_{CN}(t) + U_{Npwm}(t) \end{aligned} \quad (1)$$

and

$$\begin{aligned} U_{an}(t) &= U_{apwm}(t) - U_{npwm}(t) \\ U_{bn}(t) &= U_{bpwm}(t) - U_{npwm}(t) \\ U_{cn}(t) &= U_{cpwm}(t) - U_{npwm}(t) \end{aligned} \quad (2)$$

Let us assume the following circuit parameters:

$$L_a = L_b = L_c = L \text{ and } R_a = R_b = R_c = R \quad (3)$$

Continuous-time state equations in vector-matrix form for the three-phase four-leg VSI can be obtained by using Eqs. (1), (2), and (3). The result is shown in Eq. (4).

$$\begin{bmatrix} \frac{\mathbf{di_a(t)}}{\mathbf{dt}} \\ \frac{\mathbf{di_b(t)}}{\mathbf{dt}} \\ \frac{\mathbf{di_c(t)}}{\mathbf{dt}} \end{bmatrix} = -\begin{bmatrix} \frac{\mathbf{R}}{\mathbf{L}} & \mathbf{0} & \mathbf{0} \\ \mathbf{0} & \frac{\mathbf{R}}{\mathbf{L}} & \mathbf{0} \\ \mathbf{0} & \mathbf{0} & \frac{\mathbf{R}}{\mathbf{L}} \end{bmatrix} \begin{bmatrix} \mathbf{i_a(t)} \\ \mathbf{i_b(t)} \\ \mathbf{i_c(t)} \end{bmatrix} + \begin{bmatrix} \frac{\mathbf{1}}{\mathbf{L}} & \mathbf{0} & \mathbf{0} \\ \mathbf{0} & \frac{\mathbf{1}}{\mathbf{L}} & \mathbf{0} \\ \mathbf{0} & \mathbf{0} & \frac{\mathbf{1}}{\mathbf{L}} \end{bmatrix} \begin{bmatrix} \mathbf{U_{an}(t)} \\ \mathbf{U_{bn}(t)} \\ \mathbf{U_{cn}(t)} \end{bmatrix} - \begin{bmatrix} \frac{\mathbf{1}}{\mathbf{L}} & \mathbf{0} & \mathbf{0} \\ \mathbf{0} & \frac{\mathbf{1}}{\mathbf{L}} & \mathbf{0} \\ \mathbf{0} & \mathbf{0} & \frac{\mathbf{1}}{\mathbf{L}} \end{bmatrix} \begin{bmatrix} \mathbf{U_{AN}(t)} \\ \mathbf{U_{BN}(t)} \\ \mathbf{U_{CN}(t)} \end{bmatrix} \quad (4)$$

If we apply KCL to the points A, B, and C in Figure 1, we get current for each phase as

$$\begin{aligned} i_a(t) &= i_{ca}(t) + i_{oa}(t) \\ i_b(t) &= i_{cb}(t) + i_{ob}(t) \\ i_c(t) &= i_{cc}(t) + i_{oc}(t) \end{aligned} \quad (5)$$

Rearranging equalities in Eq. (5) in terms of state variables (capacitor voltages) and writing the resulting expressions in vector-matrix form lead to

$$\begin{bmatrix} \frac{\mathbf{dU_{AN}(t)}}{\mathbf{dt}} \\ \frac{\mathbf{dU_{BN}(t)}}{\mathbf{dt}} \\ \frac{\mathbf{dU_{CN}(t)}}{\mathbf{dt}} \end{bmatrix} = \begin{bmatrix} \frac{\mathbf{1}}{\mathbf{C}} & \mathbf{0} & \mathbf{0} & \mathbf{0} \\ \mathbf{0} & \frac{\mathbf{1}}{\mathbf{C}} & \mathbf{0} & \mathbf{0} \\ \mathbf{0} & \mathbf{0} & \frac{\mathbf{1}}{\mathbf{C}} & \mathbf{0} \end{bmatrix} \begin{bmatrix} \mathbf{i_a(t)} \\ \mathbf{i_b(t)} \\ \mathbf{i_c(t)} \end{bmatrix} - \begin{bmatrix} \frac{\mathbf{1}}{\mathbf{C}} & \mathbf{0} & \mathbf{0} & \mathbf{0} \\ \mathbf{0} & \frac{\mathbf{1}}{\mathbf{C}} & \mathbf{0} & \mathbf{0} \\ \mathbf{0} & \mathbf{0} & \frac{\mathbf{1}}{\mathbf{C}} & \mathbf{0} \end{bmatrix} \begin{bmatrix} \mathbf{i_{oa}(t)} \\ \mathbf{i_{ob}(t)} \\ \mathbf{i_{oc}(t)} \end{bmatrix} \quad (6)$$

If Eqs. (4) and (6) are combined, continuous-time state equations in vector-matrix form for the three-phase four-leg VSI in the abc coordinate system are obtained as

$$\begin{bmatrix} \frac{di_a(t)}{dt} \\ \frac{di_b(t)}{dt} \\ \frac{di_c(t)}{dt} \\ \frac{dU_{AN}(t)}{dt} \\ \frac{dU_{BN}(t)}{dt} \\ \frac{dU_{CN}(t)}{dt} \end{bmatrix} = \begin{bmatrix} i_a(t) \\ i_b(t) \\ i_c(t) \\ U_{AN}(t) \\ U_{BN}(t) \\ U_{CN}(t) \end{bmatrix} + \begin{bmatrix} U_{an}(t) \\ U_{bn}(t) \\ U_{cn}(t) \end{bmatrix} + \begin{bmatrix} i_{oa}(t) \\ i_{ob}(t) \\ i_{oc}(t) \end{bmatrix} \tag{7}$$

$U_{an}(t), U_{bn}(t), U_{cn}(t)$ are line-to-neutral output voltages and $[\mathbf{d_a}(t), \mathbf{d_b}(t), \mathbf{d_c}(t), \mathbf{d_n}(t)]$ are the modulation indices for the respective legs. Then we can write

$$\begin{bmatrix} U_{an}(t) \\ U_{bn}(t) \\ U_{cn}(t) \end{bmatrix} = U_{dc} \begin{bmatrix} d_a(t) - d_n(t) \\ d_b(t) - d_n(t) \\ d_c(t) - d_n(t) \end{bmatrix} = U_{dc} \begin{bmatrix} d_{an}(t) \\ d_{bn}(t) \\ d_{cn}(t) \end{bmatrix} = \begin{bmatrix} U_{apwm}(t) \\ U_{bpwm}(t) \\ U_{cpwm}(t) \end{bmatrix} \quad d_{abcn} \in (0,1) \tag{8}$$

Close examination of Eq. (7) reveals that expressions for phases are decoupled. For this reason, a phase can be modelled independent of the others. For example, for *phase-a* we have

$$\begin{bmatrix} \frac{di_a(t)}{dt} \\ \frac{dU_{AN}(t)}{dt} \end{bmatrix} = \begin{bmatrix} -\frac{R}{L} & -\frac{1}{L} \\ \frac{1}{C} & 0 \end{bmatrix} \begin{bmatrix} i_a(t) \\ U_{AN}(t) \end{bmatrix} + \frac{1}{L} \begin{bmatrix} 1 \\ 0 \end{bmatrix} U_{apwm}(t) - \frac{1}{C} \begin{bmatrix} 0 \\ 1 \end{bmatrix} i_{oa}(t) \tag{9}$$

$$y_a(t) = \begin{bmatrix} 0 & 1 \end{bmatrix} \begin{bmatrix} i_a(t) \\ U_{AN}(t) \end{bmatrix} \tag{10}$$

2.2. Discretization of the model of VSI

The discrete-time state space model of the system described by $\frac{dx(t)}{dt} = \mathbf{Ax}(t) + \mathbf{Bu}(t)$ and $y(t) = \mathbf{Cx}(t)$ equations is

$$x(\mathbf{k}+\mathbf{1}) = G\mathbf{x}(\mathbf{k}) + H\mathbf{u}(\mathbf{k}), \text{ where } G = \mathbf{e^{AT}}, \; H = \left[\int_0^T \mathbf{e}^{\mathbf{A}(t-\tau)} \mathbf{d}\tau\right] \mathbf{B} \tag{11}$$

$$y(\mathbf{k}) = C\mathbf{x}(\mathbf{k}) \text{ with } (\mathbf{k}) \in R^n u(\mathbf{k}) \in R^m, \tag{12}$$

where $\mathbf{x}(\mathbf{k})$ and $\mathbf{u}(\mathbf{k})$ are the discrete-time state and control vectors, and $\mathbf{T}$ is sampling interval. The full state feedback and feed forward integral controlled augmented discrete-time state space model is given in Figure 2.

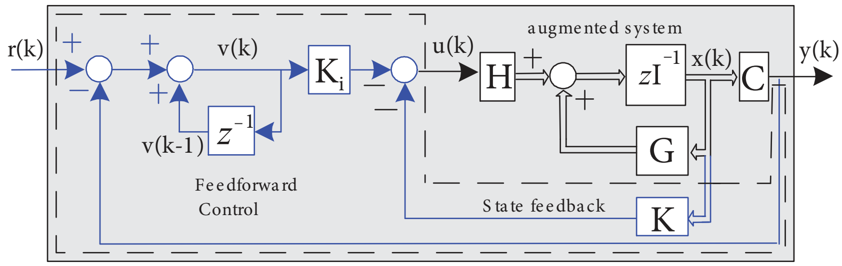

Figure 2. Augmented discrete-time model of a system.

Let the integral output $v\,(k)$ be the new state variable. Then

$$v\,(k+1) = -CGx\,(k) + v\,(k) - CHu\,(k) \tag{13}$$

The augmented discrete-time state space model for the new full state feedback and feed forward controlled system becomes

$$\begin{bmatrix} \mathbf{x(k+1)} \\ \mathbf{x(k+1)} \end{bmatrix} = \begin{bmatrix} \mathbf{G} & \mathbf{0} \\ -\mathbf{CG} & \mathbf{1} \end{bmatrix} \begin{bmatrix} \mathbf{x(k)} \\ \mathbf{v(k)} \end{bmatrix} + \begin{bmatrix} \mathbf{H} \\ -\mathbf{CH} \end{bmatrix} \mathbf{u(k)} \tag{14}$$

$$\mathbf{u\,(k)} = \begin{bmatrix} \mathbf{K} & \mathbf{K_i} \end{bmatrix} \begin{bmatrix} \mathbf{x(k)} \\ \mathbf{v(k)} \end{bmatrix} \tag{15}$$

The augmented discrete-time state space model of a three-phase four-leg VSI inverter for *phase-a* obtained by using Eqs. (14) and (15) is given by

$$\begin{bmatrix} \mathbf{i_a\,(k+1)} \\ \mathbf{U_{NA}\,(k+1)} \\ \mathbf{v(k+1)} \end{bmatrix} = \begin{bmatrix} \mathbf{0.8868} & \mathbf{-0.040} & \mathbf{0} \\ \mathbf{4.8001} & \mathbf{0.8980} & \mathbf{0} \\ \mathbf{-4.8001} & \mathbf{-0.8980} & \mathbf{1} \end{bmatrix} \begin{bmatrix} \mathbf{i_a\,(k)} \\ \mathbf{U_{NA}\,(k)} \\ \mathbf{v(k)} \end{bmatrix} + \begin{bmatrix} \mathbf{0.040} \\ \mathbf{0.102} \\ \mathbf{-0.102} \end{bmatrix} \mathbf{U_{apwm}\,(k)} \tag{16}$$

$$\mathbf{y\,(k)} = \begin{bmatrix} \mathbf{0} & \mathbf{1} & \mathbf{0} \end{bmatrix} \begin{bmatrix} \mathbf{i_a\,(k)} \\ \mathbf{U_{NA}\,(k)} \\ \mathbf{v(k)} \end{bmatrix}, \tag{17}$$

where $R = R_{abc} = 0.28\Omega, L = L_{abc} = 1.25mH, \omega = 2\pi 50 rad/s, T = 50\mu s$, and $i_{oa}\,(k) = 0A$

3. Discrete time optimal state feedback control of VSI

The three-phase four-leg VSI is completely controllable and all of the states are available for direct measurement. If the system is considered as completely state controllable, then roots of the characteristic equation may be assigned at any desired location by means of state feedback through an appropriate state feedback gain matrix [24]. If the controlled system has no integrator, the basic principle of the design of a type 1 servo system is to insert an integrator in the feed-forward path between the error comparator and the plant.

The three-phase four-leg VSI modelled in *abc* reference frame with full state feedback and integral control in discrete-time is given below.

From Figure 3, for *phase-a* the control signal $u\,(k) = u_{apwm}\,(k)$ is given by

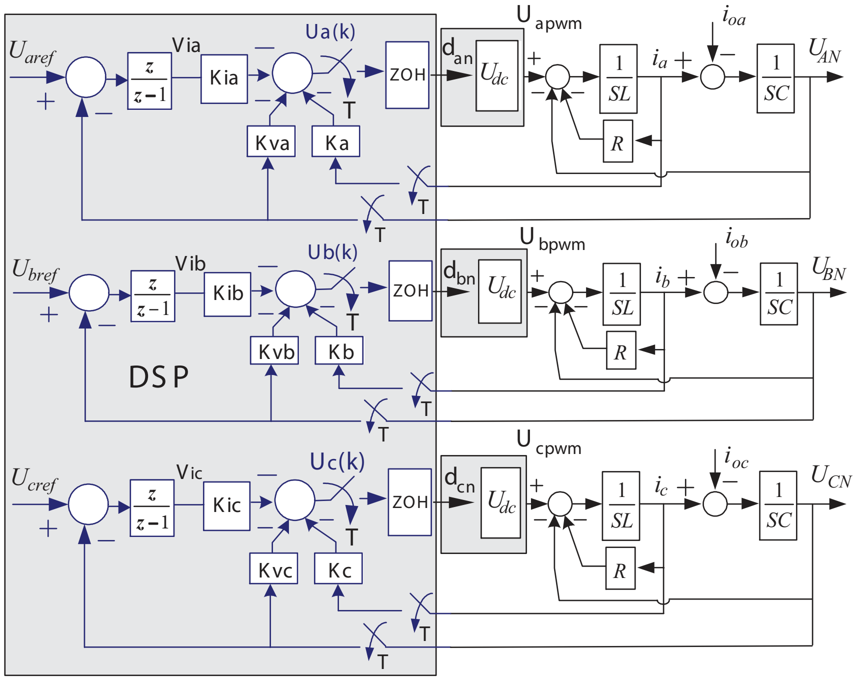

Figure 3. Full state feedback and integral control in discrete time.

$$\mathbf{u}\left(\mathbf{k}\right)=-\begin{bmatrix}\mathbf{K_a} & \mathbf{K_{va}} & -\mathbf{K_{ia}}\end{bmatrix}\begin{bmatrix}\mathbf{i_a(k)}\\ \mathbf{U_{NA}\left(k\right)}\\ \mathbf{V_{ia}(k)}\end{bmatrix} \tag{18}$$

The discrete-time state space model of the full state feedback and feed forward integral controlled system is obtained from Eqs. (16) and (18) as

$$\begin{bmatrix}\mathbf{i_a\left(k+1\right)}\\ \mathbf{U_{NA}\left(k+1\right)}\\ \mathbf{V_{ia}\left(k+1\right)}\end{bmatrix}=\begin{bmatrix}\mathbf{0.8868-0.04K_a} & \mathbf{-0.040-0.04K_{va}} & \mathbf{0.040K_{ia}}\\ \mathbf{4.8001-0.102K_a} & \mathbf{0.898-0.102K_{va}} & \mathbf{0.102K_{ia}}\\ \mathbf{-4.8001+0.102K_a} & \mathbf{-0.898+0.102K_a} & \mathbf{1-0.102K_{ia}}\end{bmatrix}\begin{bmatrix}\mathbf{i_a\left(k\right)}\\ \mathbf{U_{NA}\left(k\right)}\\ \mathbf{V_{ia}(k)}\end{bmatrix}+\begin{bmatrix}\mathbf{0}\\ \mathbf{0}\\ \mathbf{1}\end{bmatrix}\mathbf{r} \tag{19}$$

State feedback coefficients $\begin{bmatrix} K_a & K_{va} & K_{ia}\end{bmatrix}$ are obtained by solving the discrete Riccati equation such that the following performance index is minimized:

$$J=\frac{1}{2}\sum_{k=0}^{k=\infty}x\left(k\right)^TQx\left(k\right)+u\left(k\right)^TRu(k), \tag{20}$$

where R is a positive definite matrix and Q is a semipositive definite matrix.

4. 3-D SVPWM via 4 × 4 transformation matrix

In this section, the proposed 4 × $4T_{\beta\alpha0z}$ orthonormal transformation matrix in the three-phase four-leg inverter for 3-D SVPWM strategies is given and the nonzero switching space vectors from which projection matrices are determined are derived for the new matrix by using the topology in Figure 1 depending on the 16 switching cases. In the topology in Figure 1, V_{in} are inverter output phase-neutral voltages and $d_i, (i = a, b, c, n)$ are modulation indices taking values in $[0, 1]$. Then unfiltered phase voltages are found as

$$\begin{aligned} V_{an} &= V_{ag} - V_{ng} \\ V_{bn} &= V_{bg} - V_{ng} \\ V_{cn} &= V_{cg} - V_{ng} \end{aligned} \quad \mathbf{V_{ig}}= \begin{bmatrix} \mathbf{V_{ag}} \\ \mathbf{V_{bg}} \\ \mathbf{V_{cg}} \\ \mathbf{V_{ng}} \end{bmatrix} = \begin{bmatrix} 1 & 0 & 0 & 0 \\ 0 & 1 & 0 & 0 \\ 0 & 0 & 1 & 0 \\ 0 & 0 & 0 & 1 \end{bmatrix} \begin{bmatrix} \mathbf{d_a} \\ \mathbf{d_b} \\ \mathbf{d_c} \\ \mathbf{d_n} \end{bmatrix} \mathbf{u_{dc}} \tag{21}$$

$$\mathbf{V_{in}}= \begin{bmatrix} \mathbf{V_{an}} \\ \mathbf{V_{bn}} \\ \mathbf{V_{bn}} \\ \mathbf{V_{nn}} \end{bmatrix} = \begin{bmatrix} 1 & 0 & 0 & -1 \\ 0 & 1 & 0 & -1 \\ 0 & 0 & 1 & -1 \\ 0 & 0 & 0 & 0 \end{bmatrix} \begin{bmatrix} \mathbf{d_a} \\ \mathbf{d_b} \\ \mathbf{d_c} \\ \mathbf{d_n} \end{bmatrix} \mathbf{u_{dc}} \tag{22}$$

The place holder V_{nn} is defined to form a 4 × 4 transform. As can be seen from the above $\mathbf{V}_{ig}$ matrix in Eq. (21), the modulation indices of inverter legs are independent from each other. Since the matrix between $\mathbf{V}_{in}$ and $\mathbf{d}_i$ is 3 × 4, the classical 3 × 3 $T_{\beta\alpha 0}$ transformation matrix for $abc \rightarrow \alpha\beta 0$ transformation cannot be used. For this reason, the unfiltered phase voltages are obtained by using the following expression in studies in the literature:

$$\begin{bmatrix} \mathbf{V_{an}} \\ \mathbf{V_{bn}} \\ \mathbf{V_{bn}} \end{bmatrix} = \begin{bmatrix} \mathbf{d_a - d_n} \\ \mathbf{d_b - d_n} \\ \mathbf{d_c - d_n} \end{bmatrix} \mathbf{u_{dc}} \tag{23}$$

Hence, modulation indices d_a, d_b, d_c are defined in terms of d_n and the 3 × 3 $T_{\beta\alpha 0}$ transformation matrix can be used. As a new approach, $abcn \rightarrow \alpha\beta 0z$ transformation and 4 × 4$T_{\alpha\beta 0z}$ orthonormal transformation matrix are defined and used, giving rise to independence of modulation indices from d_n. Details of the 4 × 4 orthogonal transformation matrix can be found in [13,22]. The orthonormal transformation matrix $T_{\beta\alpha 0z}$ is given as

$$\mathbf{T}_{\beta\alpha\mathbf{0z}}=\sqrt{\frac{2}{3}} \begin{bmatrix} 1 & -\frac{1}{2} & -\frac{1}{2} & 0 \\ 0 & \frac{\sqrt{3}}{2} & -\frac{\sqrt{3}}{2} & 0 \\ \frac{1}{2\sqrt{2}} & \frac{1}{2\sqrt{2}} & \frac{1}{2\sqrt{2}} & -\frac{3}{2\sqrt{2}} \\ \frac{\sqrt{3}}{2\sqrt{2}} & \frac{\sqrt{3}}{2\sqrt{2}} & \frac{\sqrt{3}}{2\sqrt{2}} & \frac{\sqrt{3}}{2\sqrt{2}} \end{bmatrix} \tag{24}$$

The $T_{\beta\alpha 0z}$ matrix transforms phase-voltages space into an equivalent 3-degree of freedom (DOF) orthonormal output voltage space and V_z is defined as a placeholder for the loss of 1-DOF. The $T_{\beta\alpha 0z}$ matrix is orthonormal and invertible, i.e.$T_{\beta\alpha 0z} T_{\beta\alpha 0z}^T = I$. Therefore, the row and column vectors form a basis for the 4-DOF leg-voltage space. Let $V_{\beta\alpha 0z}$ and V_{abcn} be defined as

$$\mathbf{V}_{\beta\alpha\mathbf{0z}}= \begin{bmatrix} \mathbf{V}_\alpha & \mathbf{V}_\beta & \mathbf{V_0} & \mathbf{V_z} \end{bmatrix}^{\mathbf{T}}$$

$$\mathbf{V_{abcn}}=\begin{bmatrix} \mathbf{V_{an}} & \mathbf{V_{bn}} & \mathbf{V_{cn}} & \mathbf{V_{n}} \end{bmatrix}^{\mathbf{T}} \tag{25}$$

Then $abcn\rightarrow \alpha\beta 0z$ transformation is given below.

$$\mathbf{V_{\beta\alpha 0z}}=\mathbf{T_{\beta\alpha 0z}}\mathbf{V_{abcn}}=\sqrt{\frac{2}{3}}\begin{bmatrix} 1 & -\frac{1}{2} & -\frac{1}{2} & 0 \\ 0 & \frac{\sqrt{3}}{2} & -\frac{\sqrt{3}}{2} & 0 \\ \frac{1}{2\sqrt{2}} & \frac{1}{2\sqrt{2}} & \frac{1}{2\sqrt{2}} & -\frac{3}{2\sqrt{2}} \\ \frac{\sqrt{3}}{2\sqrt{2}} & \frac{\sqrt{3}}{2\sqrt{2}} & \frac{\sqrt{3}}{2\sqrt{2}} & \frac{\sqrt{3}}{2\sqrt{2}} \end{bmatrix}\begin{bmatrix} 1 & 0 & 0 & -1 \\ 0 & 1 & 0 & -1 \\ 0 & 0 & 1 & -1 \\ 0 & 0 & 0 & 0 \end{bmatrix}\begin{bmatrix} \mathbf{d_a} \\ \mathbf{d_b} \\ \mathbf{d_c} \\ \mathbf{d_n} \end{bmatrix}\mathbf{u_{dc}} \tag{26}$$

Rearranging the above expression gives

$$\mathbf{V_{\beta\alpha 0z}}=\begin{bmatrix} \frac{1}{\sqrt{6}}(2\mathbf{d_a}-\mathbf{d_b}-\mathbf{d_c}) \\ \frac{1}{\sqrt{2}}(\mathbf{d_b}-\mathbf{d_c}) \\ \frac{1}{2\sqrt{3}}(\mathbf{d_a}+\mathbf{d_b}+\mathbf{d_c}-3\mathbf{d_n}) \\ \frac{1}{2}(\mathbf{d_a}+\mathbf{d_b}+\mathbf{d_c}-\mathbf{d_n}) \end{bmatrix}\mathbf{u_{dc}} \tag{27}$$

$d_{\beta\alpha 0z}$ is defined as follows:

$$\begin{bmatrix} \mathbf{d_\alpha} \\ \mathbf{d_\beta} \\ \mathbf{d_0} \\ \mathbf{d_z} \end{bmatrix}=\begin{bmatrix} 2 & -1 & -1 & 0 \\ 0 & 1 & -1 & 0 \\ 1 & 1 & 1 & -3 \\ 1 & 1 & 1 & -1 \end{bmatrix}\begin{bmatrix} \mathbf{d_a} \\ \mathbf{d_b} \\ \mathbf{d_c} \\ \mathbf{d_n} \end{bmatrix} \tag{28}$$

$V_{\alpha\beta 0z}$ transform expressions can be written in terms of modulation indices as

$$\begin{bmatrix} \mathbf{V_\alpha} \\ \mathbf{V_\beta} \\ \mathbf{V_0} \\ \mathbf{V_z} \end{bmatrix}=\begin{bmatrix} \frac{1}{\sqrt{6}}\mathbf{d_\alpha} \\ \frac{1}{\sqrt{2}}\mathbf{d_\beta} \\ \frac{1}{2\sqrt{3}}\mathbf{d_0} \\ \frac{1}{2}\mathbf{d_z} \end{bmatrix}\mathbf{u_{dc}} \tag{29}$$

Switching states vectors relative to switching state can be obtained from Eq. (29) in a compact form as

$$\vec{V}_n=\vec{i}V_\alpha+\vec{j}V_\beta+\vec{k}V_0, n=0,1,2,\ldots,15 \tag{30}$$

Table 1 presents the switching combinations of d_{abcn}, their $\alpha\beta$ transformations, and 16 switching states vectors. Space vectors corresponding to 16 switching cases given in Table 1 are depicted in Figure 4a as 3-D vectors on the $\alpha\beta$ space.

Table 1. The switching combinations and switching states vectors.

n	d_{abcn}	$d_{\alpha\beta 0}$	$\vec{V}_n = \left(\vec{i}\frac{d_\alpha}{\sqrt{6}} + \vec{j}\frac{d_\beta}{\sqrt{2}} + \vec{k}\frac{d_0}{2\sqrt{3}}\right) U_{dc}$
	$nnnn$	0 0 0	$\vec{V}_0 = 0$
1	$nnnp$	0 0 −3	$\vec{V}_1 = -\frac{\sqrt{3}\vec{k}}{2} U_{dc}$
2	$nnpn$	−1 −1 1	$\vec{V}_2 = \left(-\frac{\vec{i}}{\sqrt{6}} - \frac{\vec{j}}{\sqrt{2}} + \frac{\vec{k}}{2\sqrt{3}}\right) U_{dc}$
3	$nnpp$	−1 −1 −2	$\vec{V}_3 = \left(-\frac{\vec{i}}{\sqrt{6}} - \frac{\vec{j}}{\sqrt{2}} - \frac{\vec{k}}{\sqrt{3}}\right) U_{dc}$
4	$npnn$	−1 1 1	$\vec{V}_4 = \left(-\frac{\vec{i}}{\sqrt{6}} + \frac{\vec{j}}{\sqrt{2}} + \frac{\vec{k}}{2\sqrt{3}}\right) U_{dc}$
5	$npnp$	−1 1 −2	$\vec{V}_5 = \left(-\frac{\vec{i}}{\sqrt{6}} + \frac{\vec{j}}{\sqrt{2}} - \frac{\vec{k}}{\sqrt{3}}\right) U_{dc}$
6	$nppn$	−2 0 2	$\vec{V}_6 = \left(-\frac{\sqrt{2}}{\sqrt{3}}\vec{i} + \frac{\vec{k}}{\sqrt{3}}\right) U_{dc}$
7	$nppp$	−2 0 −1	$\vec{V}_7 = \left(-\frac{\sqrt{2}}{\sqrt{3}}\vec{i} - \frac{\vec{k}}{2\sqrt{3}}\right) U_{dc}$
8	$nppp$	2 0 1	$\vec{V}_8 = \left(\frac{\sqrt{2}}{\sqrt{3}}\vec{i} + \frac{\vec{k}}{2\sqrt{3}}\right) U_{dc}$
9	$pnnp$	2 0 −2	$\vec{V}_9 = \left(\frac{\sqrt{2}}{\sqrt{3}}\vec{i} - \frac{\vec{k}}{\sqrt{3}}\right) U_{dc}$
10	$pnpn$	1 −1 2	$\vec{V}_{10} = \left(-\frac{\vec{i}}{\sqrt{6}} - \frac{\vec{j}}{\sqrt{2}} + \frac{\vec{k}}{\sqrt{3}}\right) U_{dc}$
11	$pnpp$	1 −1 −1	$\vec{V}_{11} = \left(-\frac{\vec{i}}{\sqrt{6}} - \frac{\vec{j}}{\sqrt{2}} - \frac{\vec{k}}{2\sqrt{3}}\right) U_{dc}$
12	$ppnn$	1 1 2	$\vec{V}_{12} = \left(\frac{\vec{i}}{\sqrt{6}} + \frac{\vec{j}}{\sqrt{2}} + \frac{\vec{k}}{\sqrt{3}}\right) U_{dc}$
13	$ppnp$	1 1 −1	$\vec{V}_{13} = \left(\frac{\vec{i}}{\sqrt{6}} + \frac{\vec{j}}{\sqrt{2}} - \frac{\vec{k}}{2\sqrt{3}}\right) U_{dc}$
14	$pppn$	0 0 3	$\vec{V}_{14} = \frac{\sqrt{3}\vec{k}}{2} U_{dc}$
15	$pppp$	0 0 0	$\vec{V}_{15} = 0$

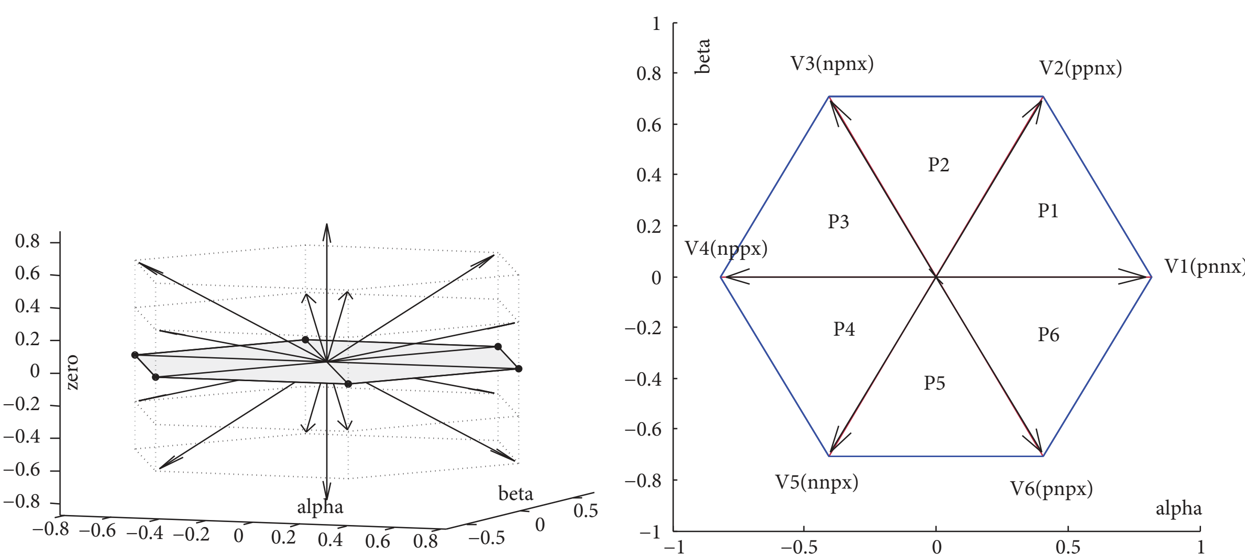

Figure 4. (a) Switching vectors in 3-D $\alpha\beta$ space; (b) Prisms of P1-P6 on $\alpha\beta$ plane.

When projected onto the $\alpha\beta$ plane, switching state vectors would form a regular hexagon as given in Figure 4b.

$$d_i = \begin{cases} p \text{ Top switch on} \\ n \text{ Bottom switch on} \end{cases} \quad i = abcn \tag{31}$$

3-D SVPWM for four-leg VSI: At any given instant, the phase voltages at the output of the four-leg VSI could be produced by an equivalent vector rotating in a 3-D space. Space vector modulation of the four-leg VSI involves identification of adjacent switching state vectors and calculation of duty cycles. Identification of adjacent vectors is a two-step process.

1-Identification of the prism number: The vectors space given in Figure 4a is divided into six triangular prisms (P1–P6) shown in Figure 4b. Let the reference vector voltage that produces the required phase voltage at the inverter output be in any prism as shown in Figure 5a. Then the algorithm used to determine the prism number is shown in Figure 5b [25].

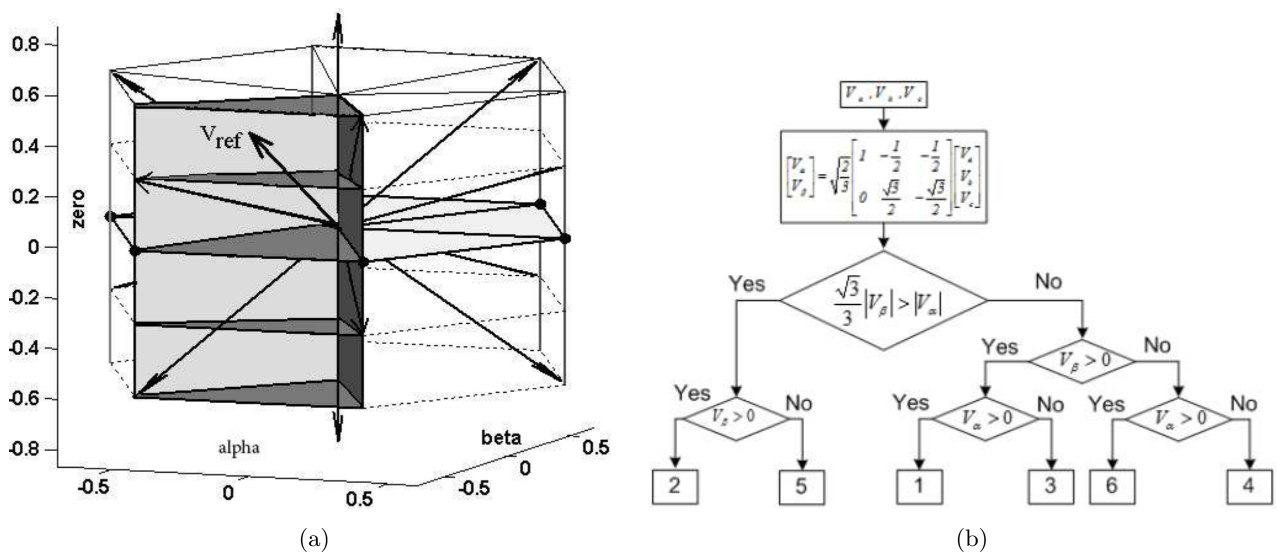

Figure 5. (a) Reference vector in prism I; (b) Identification of the prism number.

2-Identification of the tetrahedron: The second step is to determine the tetrahedron in which the reference vector is present. Each prism is divided into four tetrahedrons, leading to a total of 24 tetrahedrons. Each tetrahedron has three nonzero switching state vectors (NZSVs) and two zero switching state vectors (ZSVs). There is no mathematical expression for determining the tetrahedron containing the reference space vector in the $\alpha\beta$ space. Fortunately, based on the voltage polarities of the reference vectors in *abc* coordinate $\begin{bmatrix} \mathbf{V_{aref}} & \mathbf{V_{bref}} & \mathbf{V_{cref}} \end{bmatrix}^{\mathbf{T}}$, the tetrahedrons can be easily determined. Table 2 lists all possible polarities of the reference voltages (the required output voltage of inverter) to determine the tetrahedrons and the related three adjacent NZSVs.

Table 2. Identification of tetrahedrons.

Prisms	Tetrahedrons	Active Vectors	Condition
P1	T1	*ppnp,pnnp,pnnn*	$Va>0, Vb<0, Vc<0$
	T2	*pnnn,ppnn,ppnp*	$Va>0, Vb>0, Vc<0$
	T13	*nnnp,pnnp,ppnp*	$Va<0, Vb<0, Vc<0$
	T14	*pppn,ppnn,pnnn*	$Va>0, Vb>0, Vc>0$
P2	T3	*npnn,ppnn,ppnp*	$Va>0, Vb>0, Vc<0$
	T4	*ppnp,npnp,npnn*	$Va<0, Vb>0, Vc<0$
	T15	*nnnp,npnp,ppnp*	$Va<0, Vb<0, Vc<0$
	T16	*pppn,ppnn,npnn*	$Va>0, Vb>0, Vc>0$
P3	T5	*nppp,npnp,npnn*	$Va<0, Vb>0, Vc<0$
	T6	*npnn,nppn,nppp*	$Va<0, Vb>0, Vc>0$
	T17	*nnnp,npnp,nppp*	$Va<0, Vb<0, Vc<0$
	T18	*pppn,npnn,nppn*	$Va>0, Vb>0, Vc>0$
P4	T7	*nnpn,nppn,nppp*	$Va<0, Vb>0, Vc>0$
	T8	*nppp,nnpp,nnpn*	$Va<0, Vb<0, Vc>0$
	T19	*nnnp,nnpp,nppp*	$Va<0, Vb<0, Vc<0$
	T20	*pppn,nppn,nnpn*	$Va>0, Vb>0, Vc>0$
P5	T9	*pnpp,nnpp,nnpn*	$Va<0, Vb<0, Vc>0$
	T10	*nnpn,pnpn,pnpp*	$Va>0, Vb<0, Vc>0$
	T21	*nnnp,pnpp,nnpp*	$Va<0, Vb<0, Vc<0$
	T22	*pppn,nnpn,pnpn*	$Va>0, Vb>0, Vc>0$
P6	T11	*pnnn,pnpn,pnpp*	$Va>0, Vb<0, Vc>0$
	T12	*pnpn,pnpn,pnnn*	$Va>0, Vb<0, Vc<0$
	T23	*nnnp,pnnp,pnpp*	$Va<0, Vb<0, Vc<0$
	T24	*ppnp,pnnn,pnpn*	$Va>0, Vb>0, Vc>0$

b) Calculation of duty cycles: The reference vector V_{ref} corresponding to the active vectors related to the tetrahedron obtained in Table 2 is determined from Table 1 as

$$V_{ref} = \begin{bmatrix} V_{aref} & V_{bref} & V_{cref} \end{bmatrix}^T \tag{32}$$

Duty ratios of the switching vectors for this reference vector are given by

$$\begin{bmatrix} \mathbf{d_a} \\ \mathbf{d_b} \\ \mathbf{d_c} \end{bmatrix} = \frac{\mathbf{1}}{\mathbf{u_{dc}}} \begin{bmatrix} \mathbf{V_1} & \mathbf{V_2} & \mathbf{V_3} \end{bmatrix}^{\mathbf{-1}} \begin{bmatrix} \mathbf{V_{aref}} \\ \mathbf{V_{bref}} \\ \mathbf{V_{cref}} \end{bmatrix} \tag{33}$$

$$d_n = 1 - d_a - d_b - d_c \tag{34}$$

Inverses of 24 projection matrices $\begin{bmatrix} \mathbf{V_1} & \mathbf{V_2} & \mathbf{V_3} \end{bmatrix}^{\mathbf{-1}}$ related to the active vectors are calculated offline and a lookup table in constructed. Hence, matrix inversion is avoided in real-time applications.

As an example, let the reference vector $\begin{bmatrix} \mathbf{V_{aref}} & \mathbf{V_{bref}} & \mathbf{V_{cref}} \end{bmatrix}^{\mathbf{T}}$ be in Prism 2 and the corresponding tetrahedron be 4. From Table 2, the related switching vectors are

$$\mathbf{V_1}= \mathbf{ppnp}, \mathbf{V_2}= \mathbf{npnn}, \mathbf{V_3}= \mathbf{npnp},$$

$$\mathbf{V_0}= [\mathbf{pppp}, \mathbf{nnnn}]$$

$\begin{bmatrix} \mathbf{V_1} & \mathbf{V_2} & \mathbf{V_3} \end{bmatrix}^{-1}$ is obtained from Table 1 and the modulation indices are calculated by using the following expression:

$$\begin{bmatrix} \mathbf{d_a} \\ \mathbf{d_b} \\ \mathbf{d_c} \end{bmatrix} = \frac{\mathbf{1}}{\mathbf{u_{dc}}} \begin{bmatrix} \frac{1}{\sqrt{6}} & -\frac{1}{2\sqrt{6}} & \frac{1}{\sqrt{6}} \\ \frac{1}{\sqrt{2}} & \frac{1}{2\sqrt{2}} & 0 \\ -\frac{1}{\sqrt{3}} & \frac{1}{4\sqrt{3}} & \frac{1}{2\sqrt{3}} \end{bmatrix}^{-1} \begin{bmatrix} \mathbf{V_{aref}} \\ \mathbf{V_{bref}} \\ \mathbf{V_{cref}} \end{bmatrix} \tag{35}$$

In summary, time durations of the selected switching vectors are calculated by using 4 × 4 $T_{\alpha\beta0z}$ orthonormal transformation matrices as a new approach for 3-D SVPWM strategies. For a different reference vector V_{ref} the related prism is determined first similarly from Figure 5b. Then the corresponding tetrahedron containing V_{ref} and active switching vectors are obtained with the help of Table 2. Finally, projection matrices are determined from Table 1 and modulation indices are calculated by using Eqs. (33) and (34). Once the active vectors are determined and the duty cycles calculated, the degrees of freedom are the choice of the zero of *nnnn* or *pppp* or both, sequencing of the active vectors and splitting of the duty cycles of the vectors without introducing additional commutations.

5. Simulations and experimental results

Simulations and real-time applications consist of two parts. In the first part, general expressions of the proposed transformation matrix $T_{\alpha\beta0z}$ and all the other classical transformation matrices $T_{\alpha\beta0}$ used in the literature and the $\vec{V}_n$ switching states vector obtained for each transformation matrix are given. Transformation matrix and switching states vector general expressions are shown in Table 3 in the T and $\vec{V}_n$ arrows, respectively. On time upper switches T_a, T_b, T_c, T_z were calculated in MATLAB for balanced linear/unbalanced nonlinear three-phase voltage signals by using each transformation matrix and the same 3-D SVPWM algorithm. Phase-neutral voltages were obtained again by synthesizing T_a, T_b, T_c, T_z with DC-line voltage V_{dc} and the results were compared. T_a, T_b, T_c, T_z and $V_{an}, V_{bn}, V_{cn},$ voltage changes obtained from the simulations are given in Table 3.

As can be seen from the results in Table 3, even though the switch states vector $\vec{V}_n$ expressions are different for each transformation matrix, T_a, T_b, T_c, T_z and V_{an}, V_{bn}, V_{cn} calculated by the proposed tranformation matrix and the other classical transformation matrices are the same. Simulation results prove the validity of the proposed 4 × 4 $T_{\alpha\beta0z}$ transformation matrix for 3-D SVPWM strategies with respect to the other algorithms. Furthermore, it can also be applied to a three-phase four-leg VSI. The second study is the real-time application of 3-D SVPWM with the optimal digital control rule in three-phase four-leg in the VSI using the proposed 4 × 4 $T_{\alpha\beta0z}$ orthonormal transformation matrix. The 3-D SVPWM scheme and the optimal digital control described above were implemented on a 32-bit 150 MHz digital signal processor (DSP) TMS320F2810 in order to demonstrate the capability of the proposed method experimentally. The circuit diagram for the measurement, control, and experiment is given in Figure 6. A single discrete insulated gate bipolar transistor (IGBT) IXDH

Table 3. Verification of the proposed transformation matrix for linear and nonlinear power source voltages with simulation study.

<table>
<tr><td>T</td><td>$\sqrt{\frac{2}{3}}\begin{bmatrix}1 & -\frac{1}{2} & -\frac{1}{2}\\ 0 & \frac{\sqrt{3}}{2} & -\frac{\sqrt{3}}{2}\\ \frac{1}{\sqrt{2}} & \frac{1}{\sqrt{2}} & \frac{1}{\sqrt{2}}\end{bmatrix}$</td><td>$\frac{2}{3}\begin{bmatrix}1 & -\frac{1}{2} & -\frac{1}{2}\\ 0 & \frac{\sqrt{3}}{2} & -\frac{\sqrt{3}}{2}\\ \frac{1}{2} & \frac{1}{2} & \frac{1}{2}\end{bmatrix}$</td><td>$\frac{2}{3}\begin{bmatrix}1 & -\frac{1}{2} & -\frac{1}{2}\\ 0 & \frac{\sqrt{3}}{2} & -\frac{\sqrt{3}}{2}\\ \frac{1}{\sqrt{2}} & \frac{1}{\sqrt{2}} & \frac{1}{\sqrt{2}}\end{bmatrix}$</td><td>$\sqrt{\frac{2}{3}}\begin{bmatrix}1 & -\frac{1}{2} & -\frac{1}{2} & 0\\ 0 & \frac{\sqrt{3}}{2} & -\frac{\sqrt{3}}{2} & 0\\ \frac{1}{2\sqrt{2}} & \frac{1}{2\sqrt{2}} & \frac{1}{2\sqrt{2}} & -\frac{3}{2\sqrt{2}}\\ \frac{\sqrt{3}}{2\sqrt{2}} & \frac{\sqrt{3}}{2\sqrt{2}} & \frac{\sqrt{3}}{2\sqrt{2}} & \frac{\sqrt{3}}{2\sqrt{2}}\end{bmatrix}$</td></tr>
<tr><td>$\vec{V}_n$</td><td>$\sqrt{\frac{3}{2}}\left(\vec{\imath}\frac{d_\alpha}{3}+\vec{\jmath}\frac{d_\beta}{\sqrt{3}}+\vec{k}\frac{\sqrt{2}d_0}{3}\right)U_{dc}$</td><td>$\left(\vec{\imath}\frac{d_\alpha}{3}+\vec{\jmath}\frac{d_\beta}{\sqrt{3}}+\vec{k}\frac{d_0}{3}\right)U_{dc}$</td><td>$\left(\vec{\imath}\frac{2d_\alpha}{3}+\vec{\jmath}\frac{d_\beta}{\sqrt{3}}+\vec{k}\frac{\sqrt{2}d_0}{3}\right)U_{dc}$</td><td>$\sqrt{\frac{3}{2}}\left(\vec{\imath}\frac{d_\alpha}{3}+\vec{\jmath}\frac{d_\beta}{\sqrt{3}}+\vec{k}\frac{d_0}{3\sqrt{2}}\right)U_{dc}$</td></tr>
<tr><td colspan="3">$V_a(t) = 60\sin(\omega t)$
$V_b(t) = 60\sin(\omega t - 2.0944)$
$V_c(t) = 60\sin(\omega t - 4.1818)$</td><td colspan="2">$V_a(t) = 50\sin(\omega t) + 1.5\sin(7\omega t - 2.32) + 3\sin(11\omega t - 1.47)$
$+2\sin(13\omega t + 1.31) + 0.8\sin(17\omega t + 2.16) + 0.4\sin(19\omega t + 1.0)$
$V_b(t) = 50\sin(\omega t - 2.0944) + 1.5\sin(\omega t - 1.16)$
$V_c(t) = 30\sin(\omega t - 4.1818)$</td></tr>
<tr><td>V_{an}
V_{bn}
V_{cn}</td><td colspan="2">
</td><td colspan="2">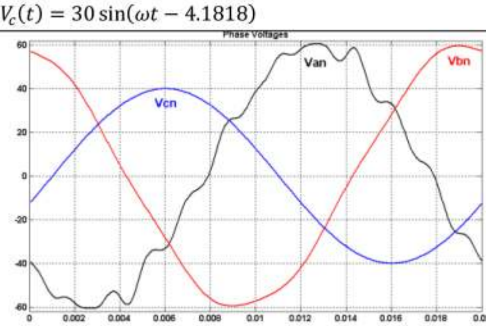
</td></tr>
<tr><td>T_a
T_b
T_c
T_z</td><td colspan="2">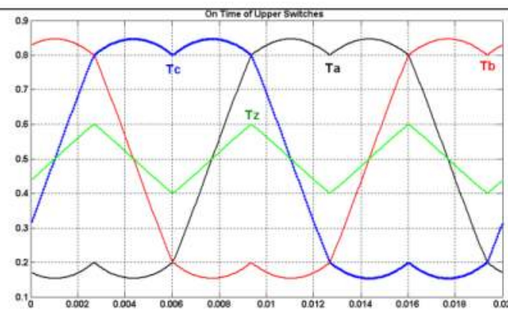
</td><td colspan="2">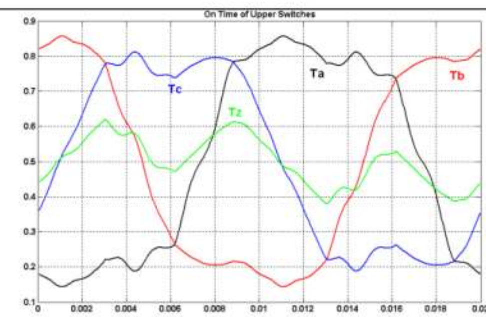
</td></tr>
</table>

30N120D1 was used as the power switching element. In the designed three-phase four-leg VSI, the inductance parameters are$R = R_{abc} = 0.28\Omega L = L_{abc} = 1.25mH$ and the capacitance value of each output capacitor is $C = C_{abc} = 10\mu F$. DC-line voltage is $V_{dc} = \sqrt{2}220V$ and the value of the capacitor connected to the DC-line is$C_{dc} = 1410\mu F$. The sampling and inverter switching frequency is$f_s = 20Khz$.

Load states, the chosen $\mathbf{Q}, \mathbf{R}$ matrices for the performance index in Eq. (20), and the state feedback coefficients calculated with respect to these matrices are given in Table 4 whether S1 and S2 switches are open or closed. Figure 6a shows the digital optimal control, hardware, and DSP used in real-time 3-D SVPWM application. The control diagram given in Figure 3 was used for all load conditions in simulations.

Finally, the simplified general control flow diagram implemented in real time is illustrated in Figure 6b. Real-time balanced linear and unbalanced nonlinear load currents sampled at $f_s = 20kHz$were used for the disturbance input signals Ioa, Iob, Ioc shown in Figure 3 in all simulations. Waveforms of optimal digital control and 3-D SVPWM for real-time applications and simulations are given in Figure 7 with $S1 = on$, $S2 = off$ in the case of balanced linear load.

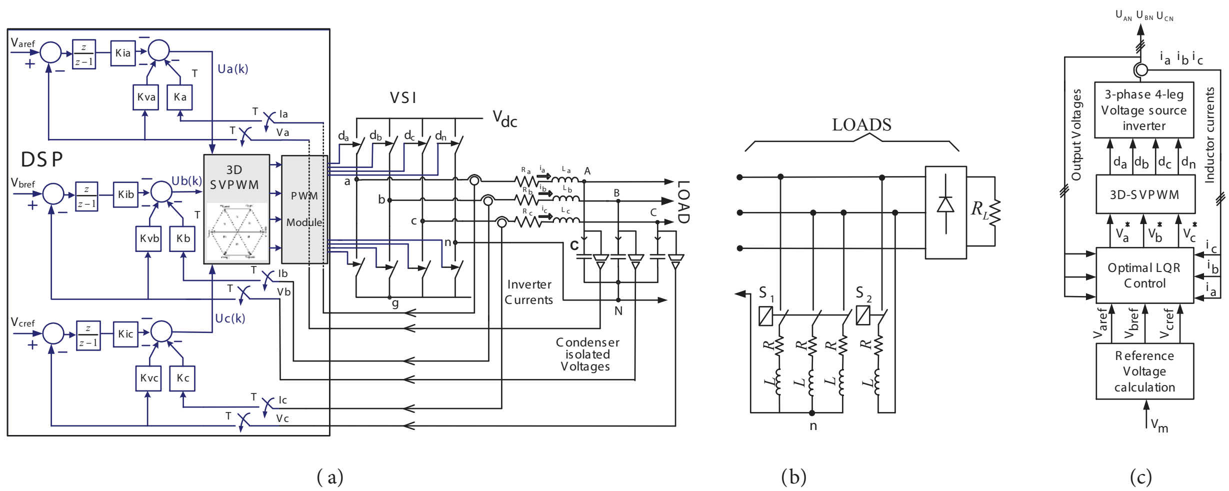

Figure 6. (a) DSP and VSI in real-time application; (b) Loads; (c) Real-time simplified control algorithm.

Table 4. Coefficients used in real-time application.

S1 S2	Load condition
on off	Balanced linear load
off on	Unbalanced nonlinear load
$Q = \begin{bmatrix} 0.01 & 0 & 0 \\ 0 & 2 & 0 \\ 0 & 0 & 0.01 \end{bmatrix}, R = [2]$	
$K_a = K_b = K_c$	6.09631
$K_{va} = K_{vb} = K_{vc}$	0.88249
$K_{ia} = K_{ib} = K_{ic}$	0.08739

Figure 7b shows the real-time balanced linear load currents. These load currents were used as disturbance inputs in simulations enabling comparison with real-time experiments under the same conditions. Real-time balanced linear load currents sampled at $f_s = 20Khz$ were used for the disturbance input signals.

In real-time application, three phase source voltages V_{an} , V_{bn} , V_{cn} and linear/nonlinear load currents I_a, I_b, I_c were sampled with $f_s = 20Khz$ sampling frequency. These samples for each phase on time of upper switches T_a, T_b, T_c, T_z obtained by 3-D SVPWM and three-phase four-leg $V_{\alpha\beta 0}$ voltages calculated by using $\mathbf{T}_{\beta\alpha\mathbf{0z}}$ transformation matrix were stored for one period in DSP RAM. Then they were used to generate in Figures 7b–7e and Figures 8b–8d given below.

The y-axis numbers seen in the waveforms in Figures 7d and 7g indicate the numbers loaded to the corresponding compare register in the PWM module of the DSP architecture to generate upper switches on times obtained by the 3-D SVPWM algorithm. Figure 8 illustrates waveforms of the digital optimal control and 3-D SVPWM algorithms for real-time applications and simulations with $S1 = off$, $S2 = on$ in the case of unbalanced nonlinear load.

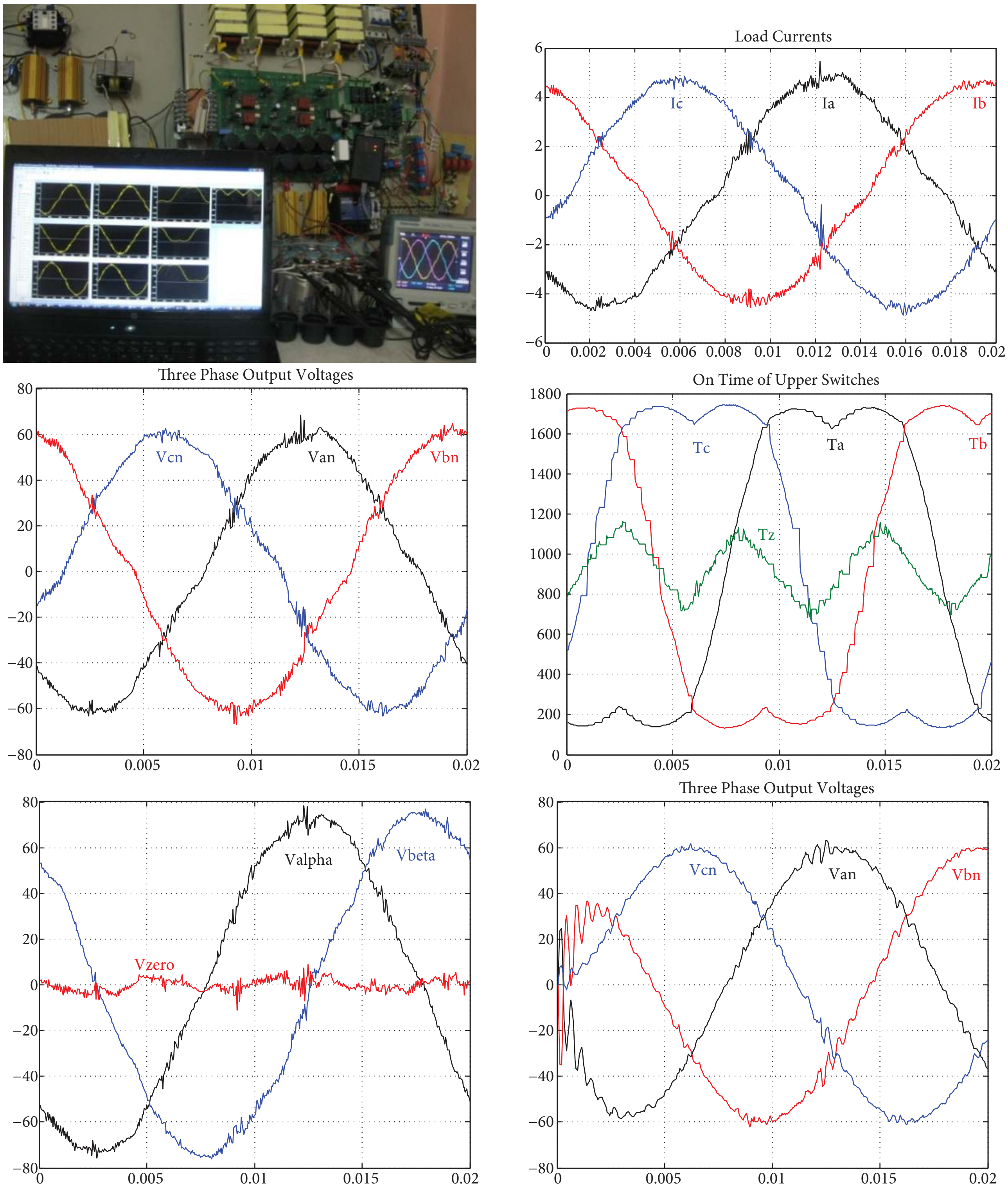

Figure 7. Real-time (a) Experimental setup; (b) Balanced linear load currents; (c) Phase-neutral voltages of the three-phase four-leg VSI; (d) On time of upper switches of the three-phase four-leg VSI; (e) Three-phase four-leg $V_{\alpha\beta 0}$ voltages. Simulation (f) Phase- neutral voltages of the three-phase four-leg VSI.

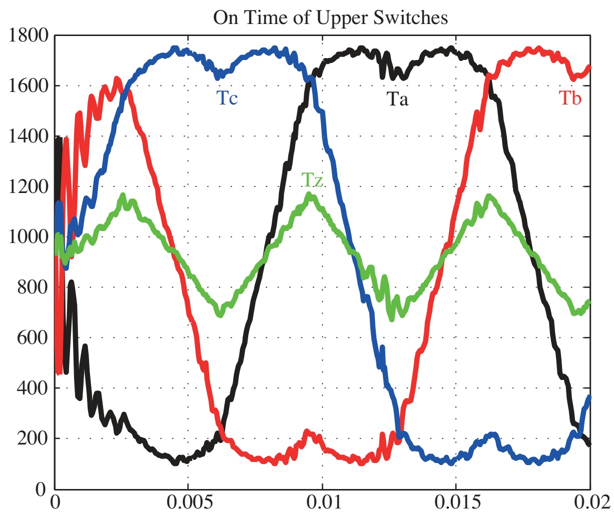

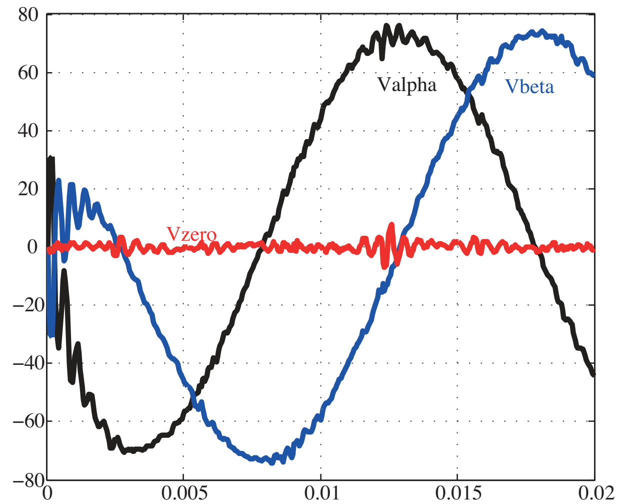

Figure 7. Real-time (g) on time of upper switches of the three-phase four-leg VSI; (h) Three-phase four-leg $V_{\alpha\beta 0}$ voltages.

Nonlinear unbalanced load in this mode contains two different loads. The first one, balanced nonlinear load, consists of a three-phase diode bridge rectifier dc load and the second was formed from a one-phase linear load connected between *phase-a* and *phase-b*. The load between the *phases-a* and *phases-b* represents one of the worst conditions under which performances of the optimal digital control and 3-D SVPWM algorithms were observed. This study considers modelling the three-phase four-leg VSI in the *abc* coordinate system, discrete-time optimal controller design, full state space feedback control of VSI, and implementation of 3-D SVPWM via 4×4 $T_{\alpha\beta 0z}$ transformation matrix. It is possible to infer the following from the real-time experimental and simulation results:

1. The model of the three-phase four-leg VSI obtained in the *abc* coordinate system can be seen to be valid from examining waveforms for real-time and simulations given in Figures 7c and 7f belonging to phase-neutral voltages for balanced sinusoidal load currents. AC signals are used directly for measurement and control since three-phase four-leg VSI modelling is carried out in the *abc* coordinate system.

2. Digital optimal controller was applied successfully in the *abc*coordinate system for the above-mentioned different load types. Modelling can be done based on dq0 reference for both modes and better results in terms of control performance can be obtained by working with DC signals after transformations.

3. That 4×4 $T_{\alpha\beta 0z}$ orthonormal transformation matrix and all classical 3×3 $T_{\alpha\beta 0}$ transformation matrices give the same results for 3-D SVPWM strategies was shown in Table 3 via simulation results obtained by using MATLAB.

4. Real-time experimental and simulation results indicate successful application of $T_{\alpha\beta 0z}$ transformation matrix 3-D SVPWM algorithms for both three-phase balanced linear and unbalanced nonlinear loads. High frequency signal components can be removed by either changing the filter structures at the output of the inverter or increasing the filter order.

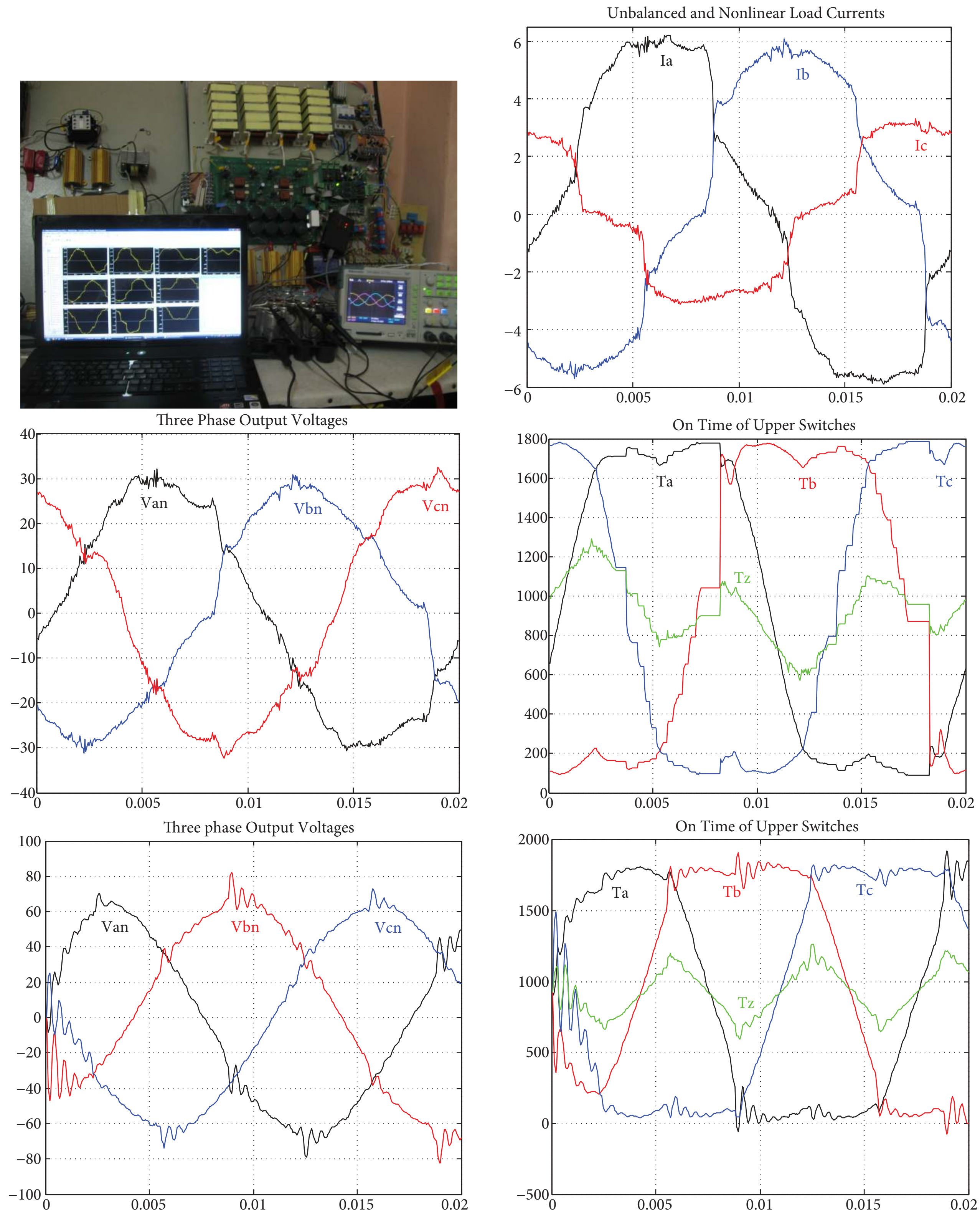

Figure 8. Real-time (a) Experimental setup; (b) Unbalanced nonlinear load currents; (c) Phase-neutral voltages of the three-phase four-leg VSI; (d) On time of upper switches. Simulation (e) Phase-neutral voltages of the three-phase four-leg VSI; (f) On time of upper switches.

6. Conclusions

This paper presents a three-phase four-leg voltage source inverter, DSP-based digital optimal controller with full state feedback, and 3-D SVPWM where the 4 × 4 $T_{\alpha\beta 0z}$ orthonormal transformation matrix is used. For 20 kHz sampling and inverter switching frequency, measurement, evolution, digital optimal control signal generation, implementation of 3-D SVPWM algorithm, and realizing on time of upper IGBTs were carried out successfully for sinusoidal three-phase four leg VSI in real-time application. Furthermore, simulation results are obtained using the new approach and all the other classical 3 × 3 transformation matrices used in the literature are given in Table 3. The accuracy of the proposed 4 × 4 transformation matrix is verified with simulation and real-time studies for linear and nonlinear power source voltages. The verification results are given in Table 3 and Figures 7 and 8, respectively.

First, the proposed orthonormal transformation matrix-based switching combinations and switching states vectors were obtained and Table 1 was created. In this way, three-phase four-leg inverter output phase-neutral voltages are calculated independently of each other by using four modulation indices. Phase-neutral voltages were obtained by synthesizing the calculated on time of the upper insulated gate bipolar transistors (IGBTs) with DC-line voltage.

Acknowledgment

This work is supported by the Scientific and Technological Research Council of Turkey (TÜBİTAK) under project number 107E165.

References

[1] Tracy J, Pfitzer H. Achieving high efficiency in double conversion transformerless UPS. In: IEEE IECON Conference; 06–10 Nov. 2005; NC, USA; pp. 942-945.

[2] Vechiu I, Curea O, Camblong H, Ceballos S, Villate S. Digital control of a three-phase four-leg inverter under unbalanced voltage conditions. In: Power Electronics and Applications Conference; 02–05 Sept. 2007; Aalborg, Denmark; pp. 1-10.

[3] Botteron F, De Camargo RF, Pinheiro H, Gründling HA, Pinheiro JR, Hey HL. On the space vector modulation and limiting algorithms for three-phase four-leg voltage source inverter in abc coordinates. In: IEEE Industrial Electronics Society Conference; 05–08 Nov. 2002; Spain; pp. 12-17.

[4] Bellini A, Bifaretti S. A simple control technique for three-phase four-leg inverters. In: International Symposium on Power Electronics (SPEEDAM); 23-26 May 2006; Italy; pp. 1143–1148.

[5] El-Barbari S, Hofmann W. Digital control of a four leg inverter for standalone photovoltaic systems with unbalanced load. In: Annual Conference of the IEEE Industrial Electronics Society (IECON); 22–28 Oct. 2000; Japan; pp. 729-734.

[6] Hongbing C, Jingyan M. Simulation research on the control strategy of three-phase four-leg inverter. In: International Conference on Computer Application and System Modeling (ICCASM). 22–24 Oct. 2010; China; pp. 602-606.

[7] Zhang X, Wang J, Li C. Three-phase four-leg inverter based on voltage hysteresis control. In: International Conference on Electrical and Control Engineering, 25–27 June 2010; China; pp. 4482-4485.

[8] Ei-Barbari S, Hofmann W. Digital control of a four leg inverter for standalone photovoltaic systems with unbalanced load. In: Industrial Electronics Society, (IECON) 26th Annual Confjerence of the IEEE, 22–28 Oct. 2000, Japan; pp. 729-734.

[9] Zhang K, Peng L, Xiong J, Chen J. State-feedback-with-integral control plus repetitive control for PWM inverters. In: Applied Power Electronics Conference and Exposition, 2005. APEC 2005, 06–10 March 2005; USA; pp. 56-62.

[10] Rech C, Pinheiro H, Gründling HA, Hey HL, Pinheiro JR. A modified discrete control law for UPS applications. J IEEE T Power Electron 2003; 18: 1138-1145.

[11] Guo W, Duan S, Kang Y. A new digital multiple feedback control strategy for single-phase voltage-source PWM inverters. In: IEEE Region 10 International Conference on Electrical and Electronic Technology (TENCON); 19–22 Aug. 2001; Singapore; pp. 809-813.

[12] Tiang TL, Ishak D. Modeling and simulation of deadbeat-based PI controller in a single-phase H-bridge inverter for stand-alone applications. Turk J Elec Eng & Comp Sci 2014; 22: 43-56.

[13] Lakshmi S, Raja SR. Observer-based controller for current mode control of an interleaved boost converter. Turk J Elec Eng & Comp Sci 2014; 22: 341-352.

[14] Kawamura A, Yokoyama T. Comparison of five different approaches for real time digital feedback control of PWM inverters. In: IEEE Industry Applications Society annual meeting; 1990; USA; pp. 1005-1011.

[15] Ryan MJ, De Doncker RW, Lorenz RD. Decoupled control of a 4-leg inverter via new 4x4 trasformation matrix. In: Power Electronics Specialists Conference (PESC), 1 Jul 1999; USA; pp. 187-192.

[16] Kim J, Sul S. A carrier-based PWM method for three-phase four-leg voltage source converters. J IEEE T Power Electron 2004; 19: 66-75.

[17] Prasad VH, Boroyevich D, Zhang R. Analysis and comparison of space vector modulation schemes for a four-leg voltage source inverter. In: IEEE APEC; 22–27 Feb 1997; Atlanta, GA, USA; pp. 864-871.

[18] Li X, Deng Z, Chen Z, Fei Q. Analysis and simplification of three-dimensional space vector PWM for three-phase four-leg inverters. J IEEE T Ind Electron 2011; 58: 450-464.

[19] Pinheiro H, Botterón F, Rech C, Schurch L, Camarago H, Hey H, Gründling H, Pinheiro J. Space vector modulation for voltage-source inverters: a unified approach. In: Annual Conference on IEEE Industrial Electronics (IECON); 05–08 Nov 2002; Sevilla, Spain; pp. 23-29.

[20] Zhang R, Prasad VH, Boroyevich D, Lee FC. Three-dimensional space vector modulation for four-leg voltage-source converters. J IEEE T Power Electron 2002; 17: 314-326.

[21] Kulaksız A, Akkaya R. Training data optimization for ANNs using genetic algorithms to enhance MPPT efficiency of a stand-alone PV system. Turk J Elec Eng & Comp Sci 2012; 20: 241-254.

[22] Perales MA, Prats M, Portillo R, J., Mora JL, León JI, Franquelo LG. Three-dimensional space vector modulation in abc coordinates for four-leg voltage source converters. IEEE Power Electron Lett 2003; 1: 104-109.

[23] Liu D, Guan M, Zhang L, Wang Y. Research on the three-phase four-leg aeronautical static inverter based on three-dimensional space vector modulation in abc coordinates. In: 9th International Conference on Electronic Measurement & Instruments; 16–19 Aug 2009; China; pp. 729-732.

[24] Ogata K. Discrete-Time Control System. Upper Saddle River, NJ, USA: Prentice-Hall Inc, 1995.

[25] Sawant RR, Chandorkar MC. A multifunctional four-leg grid-connected compensator. J IEEE T Ind Appl 2009; 45: 249-259.